https://doi.org/10.1016/j.envpol.2017.11.001

Surface O_3 photochemistry over the South China Sea: Application of a near-explicit chemical mechanism box model

Yu Wang[1], Hai Guo*, [1], Shichun Zou**, [2], Xiaopu Lyu[1], Zhenhao Ling[3], Hairong Cheng[4], Yangzong Zeren[1]

[1] Air Quality Studies, Department of Civil and Environmental Engineering, The Hong Kong Polytechnic University, Hong Kong

[2] School of Marine Sciences, Sun Yat-sen University, China

[3] School of Atmospheric Sciences, Sun Yat-sen University, China

[4]Department of Environmental Engineering, School of Resource and Environmental Sciences, Wuhan University, China

Abstract

A systematic field measurement was conducted at an island site (Wanshan Island, WSI) over South China Sea (SCS) in autumn 2013. It was observed that mixing ratios of O_3 and its precursors (such as volatile organic compounds (VOCs), nitrogen oxides (NO_x=NO+NO_2) and carbon monoxide (CO)) showed significant differences on non-episode days and episode days. Additional knowledge was gained when a photochemical box model incorporating the Master Chemical Mechanism (PBM-MCM) was applied to further investigate the differences/similarities of O_3 photochemistry between non-episode and episode days, in terms of O_3-precursor relationship, atmospheric photochemical reactivity and O_3 production. The simulation results revealed that, from non-O_3 episode days to episode days, 1) O_3 production changed from both VOC and NO_x-limited (transition regime) to VOC-limited; 2) OH radicals increased and photochemical reaction cycling processes accelerated; and 3) both O_3 production and destruction rates increased significantly, resulting in an elevated net O_3 production over the SCS. The findings indicate the complexity of O_3 pollution over the SCS.

Key words: Ozone; VOCs; Photochemical box model; Photochemistry; South China Sea

Capsule: Elevation of maritime O_3 and its precursors was attributable to the transport of polluted continental air, implying impact of human activities on atmospheric composition above the SCS.

1 Introduction

Tropospheric ozone (O_3), a major constituent of photochemical smog, is of great impact on atmospheric chemistry, human health and climate change (NRC, 1991; NARSTO, 2000; Seinfeld and Pandis, 2006). Ozone pollution is a complex phenomenon since it involves precursor emissions, photochemical formation and dynamic transport on different scales (Jacob, 1999; Guo *et al.*, 2017). With the rapid urbanization and industrialization, the Pearl River Delta (PRD) region has been experiencing severe O_3 pollution over the past decades (Chan *et al.*, 1998a, b; Ding *et al.*, 2004; Zhang *et al.*, 2007). The maximum hourly O_3 mixing ratio frequently exceeds national air quality standard (100 ppbv), mainly attributed to the elevated emissions of local precursors and regional/super-regional transport of O_3 and its precursors from other parts of China (Wang *et al.*, 2003; Guo *et al.*, 2009, 2013). Previous studies found that O_3 precursors such as volatile organic compounds (VOCs) and nitrogen oxides (NO_x=NO+NO_2) emitted in urban areas can travel to the downwind rural areas or oceanic areas, enhancing the photochemical O_3 formation in these areas (Finlayson-Pitts and Pitts, 1993; Solberg *et al.*, 2004). Ozone photochemistry in the PRD region has been documented, including VOC speciation and abundance (Lee *et al.*, 2002; Guo *et al.*, 2006, 2007, 2011; Liu *et al.*, 2008; Ou *et al.*, 2015), in-situ photochemical O_3 production (Zhang *et al.*, 2007; Lyu *et al.*, 2016a; Wang *et al.*, 2017a), process analysis of regional O_3 formation (Wang *et al.*, 2003; Zhang *et al.*, 2008; Guo *et al.*, 2009; Wang *et al.*, 2010; Jiang *et al.*, 2010; Cheng *et al.*, 2010a), atmospheric oxidative capacity (Xue *et al.*, 2016; Wang *et al.*, 2017b) and radical chemistry (Lou *et al.*, 2010; Lu *et al.*, 2012, 2014; Ling *et al.*, 2014; Lyu *et al.*, 2016b), while limited studies on O_3 formation were undertaken over the South China Sea (SCS, Wang *et al.*, 2005,

Ou Yang *et al.,* 2013). Since interaction between continental and maritime air sometimes forms weak circulation cells in which pollutants become entrained, resulting in increased concentrations, it is essential to investigate the chemical characteristics of O_3 formation over the SCS.

Although the coastline of mainland China covers approximately 14,500 km, studies of the characteristics of O_3 pollution in coastal areas are limited. Han *et al.* (2015) reported the variation of surface O_3 over the East China Sea (ECS) and found that Chinese outflows brought higher O_3 concentrations to the ECS. Ou Yang *et al.* (2013) investigated regional background O_3 level at Dongsha Island, which is located between Taiwan and the Philippines in the northern SCS. They revealed that during winter Asian monsoon, polluted air masses were delivered from the northern continent to Dongsha Island by strong northeastern winds, resulting in O_3 mixing ratios of ca. 60 ppbv. With the O_3 transport from the continent, O_3 precursors can also be transferred to the maritime atmosphere and contribute to photochemical O_3 production. However, limited studies have been carried out to improve our knowledge of photochemical O_3 formation above the ocean. One of the reasons was the lack of comprehensive precursor emissions data, especially VOC data, which hinders the investigation of mechanism of O_3 production in maritime environments. Although Wang *et al.* (2005) reported comprehensive observations of O_3 and its precursors at Tai O, a coastal site in Hong Kong, and established seasonal profiles of background air pollutants over the SCS and regional pollution of PRD, the photochemical O_3 formation in the region was not fully elaborated.

To fill the gap, continuous measurements of air pollutants, including O_3 and its precursors, were conducted at a remote island site (Wanshan Island, WSI) in the SCS from August to November 2013. A photochemical box model incorporating the Master Chemical Mechanism (v3.2) was applied to simulate the photochemical processes of local O_3 production. The

scientific objectives of this study are (1) to investigate the causes of high O_3 episodes over the SCS; (2) to understand the regime and O_3 production conditions over the SCS in order to inform policy decisions; and (3) to explore the impact of VOCs on O_3 formation pathways over the SCS.

2 Methodolgy

2.1 Sampling site

Real-time field measurements of trace gases were carried out at the WSI site in the SCS (Figure S1). The WSI site (21.93° N, 113.73° E) is about 34 km south from the coast, and is bounded to the north by the Pearl River Estuary. The distance from WSI to the urban center of Hong Kong, Macau and Zhuhai is about 64 km, 35 km and 40 km, respectively. The island has an area of 8.1 km^2 and a population of about 3000. The island has a subtropical maritime climate and is a downwind location of the PRD region in autumn and winter, when the Asian winter monsoon dominates. The measurement facilities were established on the rooftop of the National Marine Environmental Monitoring Station on Wanshan Island with a height of about 65 m above sea level and ~10 m above ground level.

2.2 Measurement methods

2.2.1 On-line measurements of O_3, CO, SO_2 and NO_x

Sampling equipment was installed in an air-conditioned room at the top floor of the National Marine Environmental Monitoring Station. A 5 m long perfluoroalkoxy (PFA) Teflon tube, with inner diameter of 9.6 mm and outer diameter of 12.7 mm, was used as a sampling tube. The inlet of the sampling tube was 2 m above the rooftop of the building, while the other end was coupled to a PFA manifold which linked together all the gas analyzers in the room. A bypass pump connected to the manifold drew ambient air at a rate of 5 L min^{-1} into the intakes of the gas analyzers.

Trace gases including O_3, NO_x, CO and SO_2 were simultaneously monitored during the sampling period (11 August – 22 November, 2013). Briefly, the target pollutants were measured with commercial analyzers developed by Advanced Pollution Instrumentation (API) Inc. A UV photometric analyzer (API model 400E with a detection limit of 0.6 ppbv) was used to monitor O_3, while NO-NO_2-NO_x was measured with a chemiluminescence analyzer (API model 200E with a lower detectable limit of 0.4 ppbv) equipped with a replaceable molybdenum-converter cartridge. A gas filter correlation trace level CO analyzer (API model 300EU with a detection limit of 0.02 ppmv) with a heated, platinum CO scrubber to correct its baseline was utilized to measure CO, and SO_2 was detected with a pulsed UV fluorescence monitor (API model 100E with a detection limit of 0.4 ppbv). In addition, meteorological parameters (solar radiation, temperature, relative humidity, wind speed and wind direction) were continuously measured by a weather station (Vantage Pro 2, Davis Inc).

For quality control, a transfer standard (Thermo Environmental Instruments (TEI), 49PS) was used to calibrate the O_3 analyzer. For CO, SO_2 and NO, NIST (National Institute of Standards and Technology)-traceable standard (Scott-Marrin, Inc.) was diluted using a dynamic calibrator (Environics, Inc., Model 6100). The standard contained 156.5 ppm CO (±2 %), 15.64 ppm SO_2 (±2 %), and 15.55 ppm NO (±2 %). Through injecting scrubbed ambient air (TEI, Model 111) and a span gas mixture, these analyzers were calibrated. In addition, a data logger (Environmental Systems Corporation, Model 8832) was used for calibration control and data collection, with a time resolution of 1 min intervals (Guo *et al.*, 2013).

2.2.2 VOCs sampling and analysis

Intermittent whole-air canister samples for VOCs and carbonyl cartridge samples for aldehyldes were obtained at WSI for 8 O_3 episode days and 13 non-O_3 episode days. The O_3 episode days were defined as the days with maximum hourly average O_3 value exceeding 100 ppbv (China's Grade II Standard). Specifically, the 13 non-O_3 episode days included 11-12,

18, 26 September, 9-10, 17, and 30-31 October, and 18-21 November 2013, while the 8 O_3 episode days were 2-4 and 22-25 October, and 15 November 2013. The whole-air samples were collected using evacuated 2-L electro-polished stainless steel canisters. The canisters were cleaned, conditioned and evacuated before sampling. A flow-restrictor was used to collect air samples over 1-hour integration. Seven 1-hr VOC samples (every two hours from 7:00 – 19:00 LT inclusive) were collected on each of the 13 non-O_3 episode days and the 8 O_3 episode days at the site with additional samples collected at 01:00, 03:00, 05:00 and 21:00 on episode days. The speciation and abundance of individual VOCs in the canisters were determined by gas chromatography (GC) with flame ionization detection (FID), and GC with electron capture detection (ECD) and mass spectrometer detection (MSD). 59 C_2-C_{11} hydrocarbon species were quantified. The detection limits of VOCs ranged from 3 to 57 pptv with a measurement precision of 2-5%, and a measurement accuracy of 5%. Detailed descriptions of the analysis system, quality control and quality assurance for VOC samples are provided elsewhere (Simpson *et al.*, 2010; Zhang *et al.*, 2012).

Furthermore, 2h carbonyl cartridge samples were simultaneously collected every two hours during 07:00-19:00 using acidified 2,4-dinitrophenylhydrazine (DNPH) silica cartridges at a flow rate of 0.4-0.6 L min^{-1}. The procedures including the pretreatment, the configuration of the analysis system, and the methods of the quality control and quality assurance for carbonyl samples can be found in detail elsewhere (Guo *et al.*, 2009). Briefly, the carbonyl samples were analyzed using high performance liquid chromatography (HPLC) with an auto-sampler. The identification and quantification were on the basis of retention times and peak areas of the corresponding calibration standards. Five standard concentrations, covering the concentrations of interest for ambient air, were selected to calibrate the instrument. Typically, 11 C_1–C_9 carbonyl compounds were quantified with a detection limit of ~0.2 ppbv and a measurement precision of ~10%.

2.3 Photochemical box model (PBM)

2.3.1 General description

In this study, the photochemical formation of O_3, free radicals and intermediate products at WSI on 8 O_3 episode days and 13 O_3 non-episode days were simulated using a photochemical box model incorporating the Master Chemical Mechanism (PBM-MCM). The MCM adopts a near-explicit mechanism, involving 5,900 chemical species and around 16,500 reactions including the reaction between radicals (*i.e.*, OH) and SO_2 (Long *et al.*, 2017). Since methane and tropospheric molecular hydrogen account for a significant fraction of the OH to HO_2 conversion in the background atmosphere, their roles in the model are considered and their values are set to be 1.95 ppmv and 0.5 ppmv, respectively, according to our past observations (Ling *et al.*, 2014; Lyu *et al.*, 2015a). Previous studies show that it performs well in calculating the O_3 production (Jenkin *et. al.*, 1997, 2003; Saunders *et. al.*, 2003).

Different from the photochemical trajectory model (PTM) with MCM which is based on emission inventories (Cheng *et al.*, 2010a; Derwent, 2017), in this study the observed values of air pollutants (O_3, NO_x, CO, SO_2 and 51 VOCs, see Table S1) and meteorological parameters (temperature and relative humidity) between 0700 and 1900 were used to constrain the model (Guo *et al.*, 2013; Ling *et al.*, 2014; Lyu *et al.*, 2015a, b). It is noteworthy that since trace gases and metrological parameters were measured in minute intervals, they were averaged to hourly values prior to model input. One of the purposes is to minimize the influence of variations within an hour as the levels of reactive pollutants would vary from their initial hourly values by the end of each hour due to radical oxidation. Because the VOCs and OVOCs were measured at 2-hourly intervals, a method based on the mass conservation of a species inside a fixed Eulerian box was utilized to obtain hourly VOC and OVOC profiles from the limited samples (Zhang *et al.*, 2007; Lyu *et al.*, 2016a). In addition, model sensitivity tests on the

174 measurement uncertainties of NO_x and VOCs showed negligible impact on the simulated O_3
175 production (Figures S2 and S3).

176 Apart from the chemical reactions, the model considered other modules such as photolysis rate,
177 dry deposition and the boundary layer height. The photolysis rates of different chemicals in the
178 model were parameterized using the photon flux determined from the Tropospheric Ultraviolet
179 and Visible Radiation (TUVv5) model (Lam *et al.*, 2013), while the dry deposition module
180 included the dry deposition of air pollutants, which were parameterized as an average
181 deposition rate within the mixed layer height (MLH). The MLH was assumed to vary from 300
182 m at night to 1400 m during the daytime (Lam *et al.*, 2013). Sensitivity runs with MLHs of 900
183 m and 1900 m (1400 ± 500 m) indicated that its impact on O_3 simulation was minor (<3%)
184 (Figure S4). It should be noted that the PBM-MCM model did not consider physical processes,
185 *i.e.*, vertical and horizontal transport.

186 Facsimile software (Curtis and Sweetenham, 1987) was used to integrate the model system of
187 differential equations with integration output set each hour. The model output included the
188 simulated mixing ratios of O_3, radicals and intermediates. More detailed descriptions of the
189 PBM-MCM are provided in Ling *et al*. (2014), Guo *et al*. (2013) and Cheng *et al*. (2010a).

190 2.3.2 Photolysis rates in the model

191 Since direct measurements of $j(O^1D)$ and $j(NO_2)$ were not obtained during this sampling
192 campaign, the measured total solar radiation was applied to calibrate the photolysis frequencies
193 by comparing with the simulation results of the TUVv5 model
194 (http://cprm.acom.ucar.edu/Models/TUV/Interactive_TUV/). In the online TUVv5 model, the
195 surface albedo of 0.1 and the overhead O_3 column density of 323 Dobson units were applied.
196 The calculated solar radiation was obtained by regulating the parameter of optical depth to get
197 close to the measurements, while the photolysis frequencies were provided by the online TUV

model using the same physical parameters. Then, the PBM-MCM model used the calibrated TUV photolysis frequencies to simulate the photochemical reactions.

2.3.3 Model performance

The index of agreement (IOA), which indicates the matching degree between the simulated and observed O_3 (Equation 1), was used to evaluate the model performance (Huang *et al.*, 2005; Lyu *et al.*, 2015a; Wang *et al.*, 2015).

$$\mathrm{IOA} = 1 - \frac{\sum_{i=1}^{n}(O_i - S_i)^2}{\sum_{i=1}^{n}(|O_i - \bar{O}| + |S_i - \bar{O}|)^2} \quad \text{(Eq. 1)}$$

where S_i and O_i are simulated and observed hourly values, respectively, $\bar{o}$ represents the average observed values, and n is the sample number. The range of IOA is 0~1. The higher the IOA value is, the better agreement between simulated and observed values is (Huang *et al.*, 2005).

2.3.4 Estimate of relative incremental reactivity (RIR)

The sensitivity of O_3 formation to precursors was assessed using the relative incremental reactivity (RIR), which was calculated from the output parameters of the PBM-MCM (Cardelino and Chameides, 1995). RIR reflects the relative variation in O_3 production rate for a change of mixing ratios in precursors. A larger positive RIR of a given precursor indicates a higher probability that O_3 production will be more significantly reduced by cutting down emissions of this precursor. The calculation of RIR values refers to the following equation:

$$\mathrm{RIR}(X) = \frac{[P^{S}_{O_3\text{-}NO}(X) - P^{S}_{O_3\text{-}NO}(X - \Delta X)]/P^{S}_{O_3\text{-}NO}(X)}{\frac{\Delta S(X)}{S(X)}} \quad \text{(Eq. 2)}$$

X is a specific precursor (*i.e.*, VOCs, NO_x, or CO); S(X) is the observed mixing ratio of precursor X (ppbv); ΔS(X) is the hypothetical change of mixing ratio of X; $P^{S}_{O_3-NO}(X)$ is the

net O_3 production in a base run with original mixing ratios, while $P^S_{O_3-NO}(X-\Delta X)$ is the net O_3 production in a second run with a hypothetical change ($\Delta S(X)$) (10% in this study). Ozone titration by NO was considered in both runs. The O_3 production $P^S_{O_3-NO}$ was calculated according to Eq. 3 - Eq. 5. The superscript "S" represents the specific sampling site, which is WSI site in this study. Detailed calculation method is provided in Ling *et al.* (2014).

2.3.5 Simulation of photochemical pathways and radicals

The net O_3 production ($P_{O_3\text{-}NO}$) was the difference between O_3 gross production ($G_{O_3\text{-}NO}$) and O_3 destruction ($D_{O_3\text{-}NO}$) (Equation 3). $G_{O_3\text{-}NO}$ was calculated by the oxidation of NO by HO_2 and RO_2 (Equation 4), while $D_{O_3\text{-}NO}$ was calculated by O_3 photolysis and reactions of O_3 with OH and HO_2 (Equation 5). Among Equations 3-5, O^3P, O^1D, NO and NO_2 were put into instantaneous steady state. All radicals and intermediates were obtained from the outputs of the PBM-MCM. The constants (k) represent the rate coefficients of corresponding reactions, respectively. The superscript '*i*' in equation 4 refers to individual RO_2.

$$P_{O_3-NO} = G_{O_3-NO} - D_{O_3-NO} \quad \text{(Eq. 3)}$$

$$G_{O_3\text{-}NO} = k_{HO_2+NO}[HO_2][NO] + \sum k_{RO_{2i}+NO}[RO_{2i}][NO] \quad \text{(Eq. 4)}$$

$$D_{O_3\text{-}NO} = k_{HO_2+O_3}[HO_2][O_3] + k_{OH+O_3}[OH][O_3] + k_{O(^1D)+H_2O}[O(^1D)][H_2O] + k_{OH+NO_2}[OH][NO_2] + k_{alkenes+O_3}[alkenes][O_3] \quad \text{(Eq. 5)}$$

3 Results and discussion

3.1 General features

An overview of this sampling campaign from August to November was given by Wang *et al.* (2017b). In this study, we mainly focused on the 8 O_3 episode days and 13 non-O_3 episode days at WSI when trace gases, VOCs and OVOCs were all monitored. Table 1 presents the statistical description of O_3, CO, SO_2, NO, NO_2 and TVOCs during the 8 O_3 episode days and 13 non-

O_3 episode days at WSI. The TVOCs was defined as the sum of 70 measured VOC species (Table S1). It was found that both O_3 and its precursors had higher mixing ratios on O_3 episode days than on non-O_3 episode days (p<0.05), partly due to different meteorological conditions during the two periods. Figure S5 displays the mean wind fields on O_3 episode and non-O_3 episode days at WSI. North winds dominated during episodes, which transported dirty continental air masses to the maritime site, leading to elevated levels of air pollutants. In contrast, the winds turned to be eastern direction on non-O_3 episode days, which brought less polluted maritime/coastal air to the site, resulting in low mixing ratios of air pollutants. Moreover, since O_3 photochemistry is closely associated with the speciation and abundance of its precursors, the different levels and compositions of O_3 precursors may alter the photochemical pathways and subsequently the O_3-precursor relationships and O_3 production between O_3 episode and non-O_3 episode days in the maritime atmosphere. As such, the O_3 photochemistry on O_3 episode and non-O_3 episode days over the SCS was elaborated using the PBM-MCM model below.

Table 1. Statistical description of air pollutants on O_3 episode and non-O_3 episode days at WSI (unit: ppbv; S.D.: standard deviation)

	Episode		Non-episode	
	Average ± S.D.	Maximum	Average ± S.D.	Maximum
O_3	74.1±34.2	152.3	53.6±15.1	81.5
CO	410±80	640	210±10	420
NO	0.6±1.0	5.5	0.4±0.9	8.5
NO_2	7.1±5.3	28.5	1.9±3.1	17.5
SO_2	4.4±1.9	8.8	2.1±1.0	6.4
TVOCs	26.3±9.8	74.8	15.5±7.1	39.3

3.2 Model verification

Prior to the study of local O_3 formation mechanisms, the PBM-MCM model performance was evaluated. Figure 1 compares day-to-day patterns of simulated and observed O_3 on the 21 days. It was clear that the model well simulated the O_3 variations, which started to increase in the morning, reached peak value in the afternoon, and then decreased to low values in the evening. The discrepancy of daily extremes (*i.e.*, maximums and minimums) between the simulated and observed values was ±20%. The simulated values were generally lower than the observations and the IOA of the 21-day simulation was 0.73, in line with the IOA values for the O_3 simulations of other models (0.68 – 0.89) (Wang *et al.*, 2015; Lyu *et al.*, 2015a, b, 2016a, b; Wang *et al.*, 2017a), suggesting that the model performance on O_3 simulation in this study was acceptable.

The difference between the observations and simulation results was partly because the physical processes in the atmosphere, such as horizontal and vertical transport, were not considered in the PBM-MCM. The speculation is reasonable because the PBM-MCM was mainly simulating local O_3 production, while the vertical and horizontal transport was related to regional transport which was demonstrated weaker on episode days than on non-episode days in the study region, leading to lower model-observation agreement on non-episode days (Wang *et al.*, 2017b; Guo *et al.*, 2013; Ding *et al.*, 2004). In addition, other factors such as uncertainty of measured precursors, mixed layer height set-up in the model, and "spin-up" time might also influence the model-observation agreements. For example, since the VOCs and OVOCs were intermittently measured in this study, a "spin-up" time before the modeling days was not applied in the model to get the radical intermediates steady which might have caused a slight underestimation of the simulated O_3 production and its sensitivity to precursors (Wang *et al.*, 2017a).

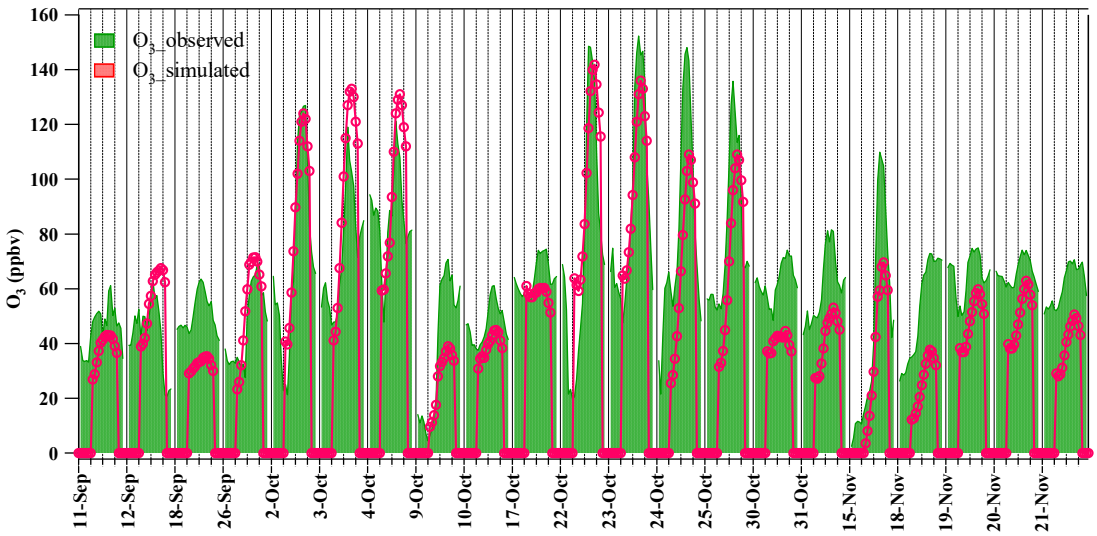

278

279 Figure 1. Simulated and observed O_3 on the 21 sampling days at WSI.

280 3.3 O_3-precursor relationships

281 To understand the causes of O_3 formation at a given site, O_3-precursor relationships were first
282 investigated. Figure 2 shows the average RIR values on non-O_3 episode and O_3 episode days
283 at WSI. During non-O_3 episode days, the RIR values of all precursors were positive while NO_x
284 had the highest RIR value (0.64±0.05), and other precursors, *i.e.*, anthropogenic VOCs
285 (AVOCs, 48 species for model input), biogenic VOCs (BVOCs, *i.e.*, isoprene and *α/β*-pinenes.
286 See further classification in Table S1) and CO, all had values lower than 0.1, suggesting that
287 O_3 production responded most sensitively to NO_x and less to VOC and CO, implying a NO_x
288 limited regime. The result was consistent with previous studies that O_3 production was both
289 NO_x and VOC limited (transition regime) at a rural site of Guangzhou (Backgarden) in the
290 inland PRD region (Lu *et al.*, 2010).

291 In comparison, on O_3 episode days AVOC had the highest RIR value (0.54±0.04) while the
292 values of BVOC and CO were lower than 0.2, implying that the O_3 formation was sensitive to
293 AVOC, *i.e.*, VOC limited. Moreover, the RIR value of NO_x was negative (-0.17±0.02),

suggesting that cutting NO_x would increase the O_3 formation. The RIR patterns during episodes were similar to previous results obtained at different urban sites in Hong Kong (Cheng *et al.*, 2010b; Ling *et al.*, 2013; Guo *et al.*, 2013) and in the inland PRD region (Zhang *et al.*, 2007; Lu *et al.*, 2010).

In summary, the O_3-precursor relationships over the SCS suggest that controlling NO_x emissions during non-episode days is more effective to O_3 reduction, while controlling VOC emissions on episode days results in the mitigation of O_3 formation at the site. The different O_3 control regimes between non-O_3 episode and O_3 episode days reveal the variations of chemical compositions during these two different events though the reasons warrant further investigation.

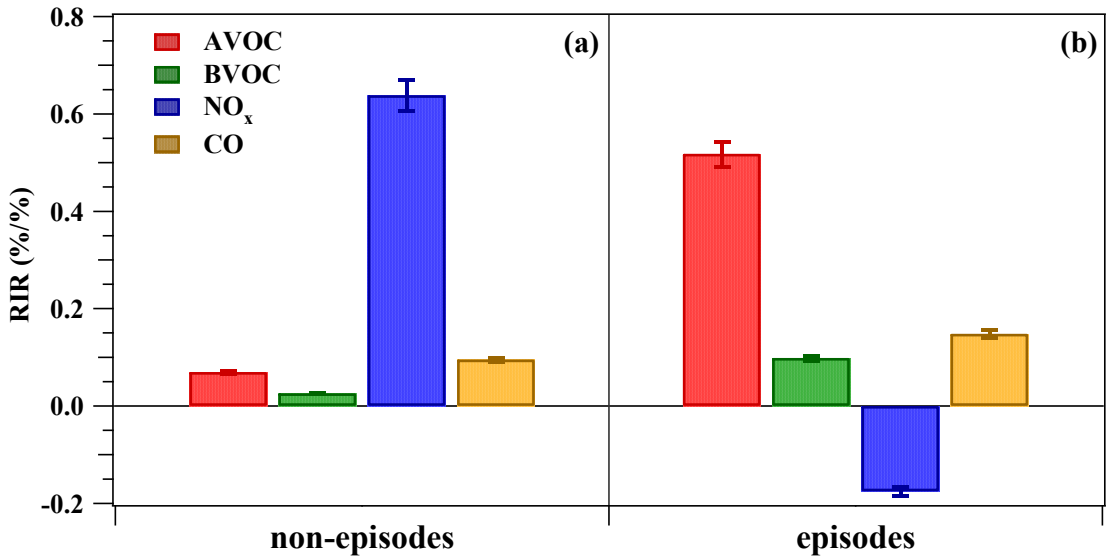

Figure 2. RIR values of O_3 precursors, *i.e.*, AVOC, BVOC, NO_x and CO at WSI on (a) O_3 non-episode days and (b) O_3 episode days. Error bars are the 95% C. I. of the averages. Higher RIR value of a precursor indicates that O_3 formation is more sensitive to it, whereas a negative RIR value of a precursor implies that cutting it will increase the O_3 formation.

The sensitivity of O_3 formation to individual VOC species was further evaluated. Figure 3 presents the top 10 AVOC species (as determined by their RIR values) at WSI on non-O_3

episode days and O_3 episode days. It is noteworthy that isoprene was ranked No. 2 based on its RIR value. However, since it is a BVOC, it is omitted in Figure 3. The results indicated that though 51 VOC species were input into the PBM-MCM, the summed RIR values of top 10 AVOC species and isoprene occupied 77% and 13% of the overall RIR values at WSI, respectively, reflecting that O_3 formation over the SCS was ascribed to a minority of VOC species.

In comparison, all 10 AVOC species had much higher RIR values on O_3 episode days, implying that controlling these VOC species would be more effective to limit O_3 formation on episode days. Furthermore, the top 4 VOC species were the same on non-O_3 episode days as those during episodes, indicating that control measures should always concentrate on these VOC species to reduce O_3 pollution over the SCS. In addition, the RIR value of formaldehyde (an oxygenated VOC (OVOC) species) was much higher than others on episode days, suggesting important contribution of OVOC to O_3 formation in the maritime atmosphere.

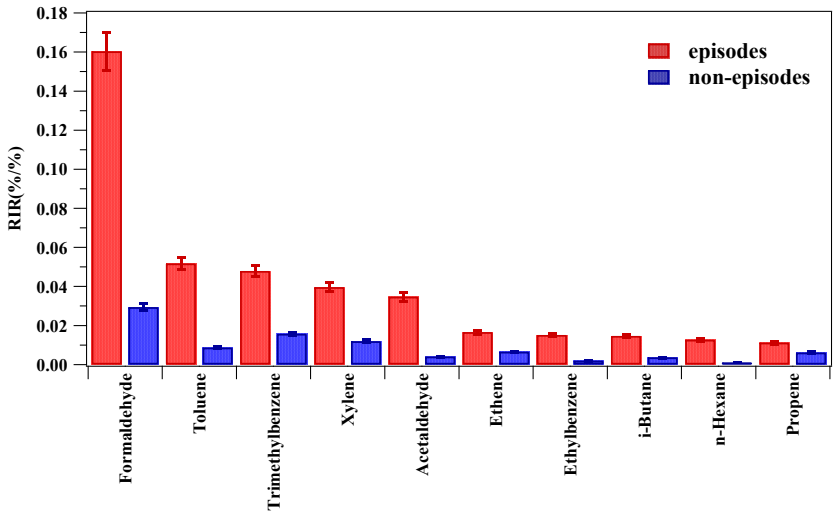

Figure 3. Average RIR values of top 10 AVOC species at WSI on non-O_3 episode days (blue) and episode days (red). The top 10 AVOC species are determined by their RIR values. Error bars indicate the 95% C. I. of the averages.

3.4 O_3 photochemistry

3.4.1 Photochemical cycling

Ozone formation involves a series of complex reaction cycles of radicals (such as OH, HO_2, and RO_2) in which CO and VOCs are continually oxidized. Briefly, OH radicals initially oxidize the precursors (*i.e.*, VOCs, CO and NO_x) and result in O_3 formation. The cycling between OH and HO_2 accelerates the chain-propagation reactions (see Text S1 in the Supplementary for further description). Therefore, the concentrations and cycling of OH and HO_2 are important parameters affecting O_3 photochemistry.

Figure 4 shows the average variations of simulated OH and HO_2 on non-O_3 episode and O_3 episode days at WSI. The maximum concentrations of OH and HO_2 were respectively 9.2×10^6 and 4.7×10^8 molecules cm^{-3} (equivalent to 0.37 and 19 pptv, respectively) on episode days, and 4.9×10^6 and 5×10^8 molecules cm^{-3} (0.2 and 20 pptv) on non-episode days, respectively. The average OH mixing ratio during episodes ($4.2 \pm 1.1 \times 10^6$ molecules cm^{-3}) was about 70% higher ($p<0.05$) than that during non-O_3 episodes ($2.5 \pm 0.8 \times 10^6$ molecules cm^{-3}), reflecting higher photochemical reactivity on episode days. In contrast, the average HO_2 mixing ratio during episodes ($2.2 \pm 0.9 \times 10^8$ molecules cm^{-3}) was comparable ($p>0.05$) to that during non-O_3 episodes ($2.6 \pm 0.6 \times 10^8$ molecules cm^{-3}). The larger variations of OH and HO_2 levels before 13:00 during episodes were likely due to larger variations of mixing ratios of NO_x in the morning (see Figure S6), which affected radicals through the reactions of HO_2+NO, OH+NO and OH+NO_2.

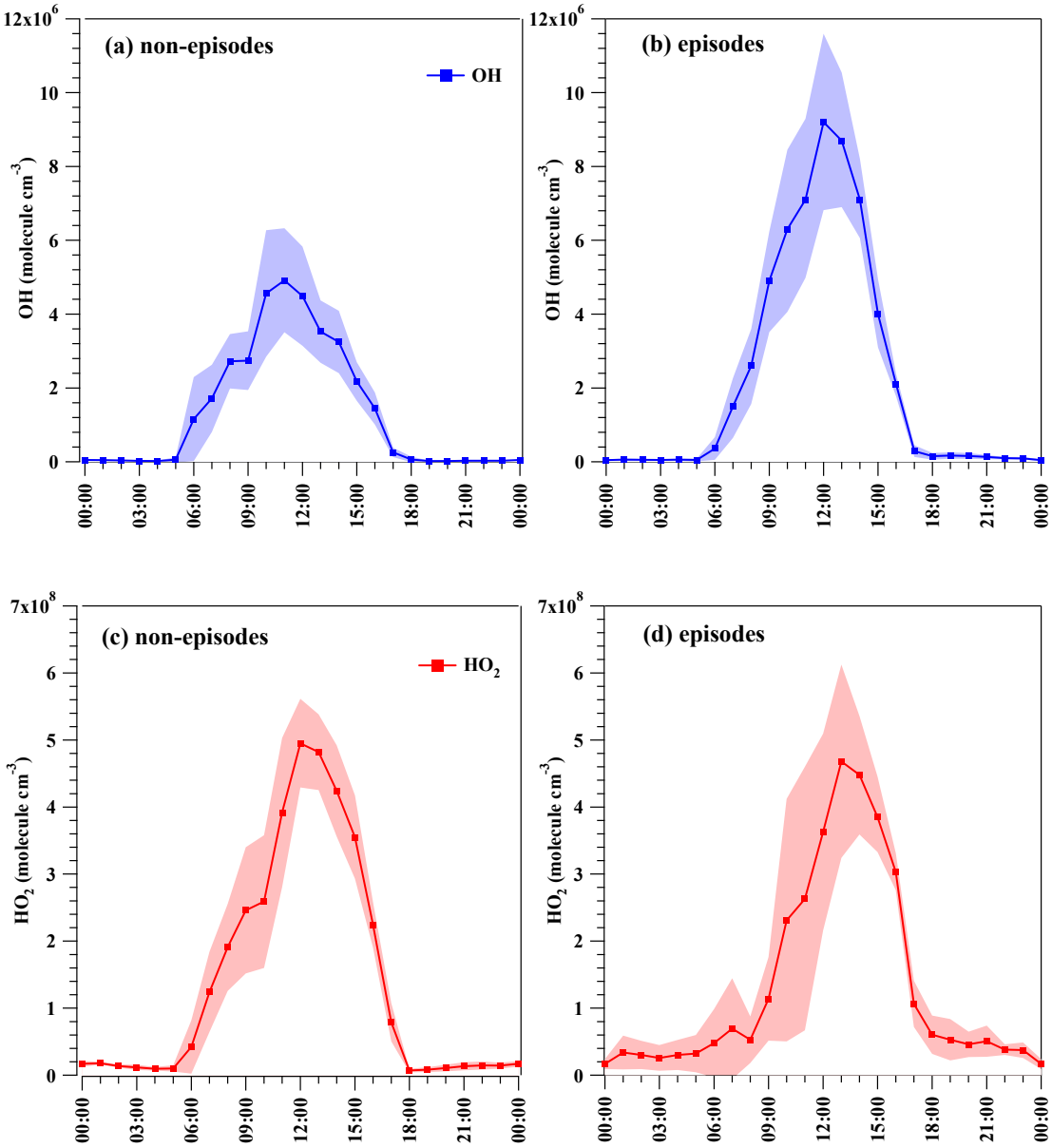

Figure 4. Simulated average temporal variations of OH on (a) non-O_3 episode days and (b) O_3 episode days, and HO_2 radicals on (c) non-O_3 episode days and (d) O_3 episode days at WSI. The shaded area indicates the 95% confidence interval of the data.

Figure 5 illustrates the predominant production and loss pathways of OH and HO_2 on non-O_3 episode days and episode days at WSI. In general, the overall formation or loss rates of OH

355 and HO_2 during episodes ($10.3\pm0.9\times10^7$ and $9.0\pm2.3\times10^7$ molecules cm^{-3} s^{-1}, respectively)
356 were much higher than those on non-episode days ($3.3\pm1.4\times10^7$ and $3.1\pm0.7\times10^7$ molecules
357 cm^{-3} s^{-1}, respectively) ($p<0.05$), suggesting more efficient radical cycling on episode days (see
358 Text S1 in the Supplementary for further description of radical cycling).

359 Specifically, during non-O_3 episodes, the reaction of HO_2+NO was the most predominant
360 pathway to generate OH, followed by O_3 photolysis, HONO photolysis and ozonolysis of
361 alkenes, with contributions of 75%, 18%, 5% and 2 %, respectively (Figure 5a). In contrast,
362 OH was mainly consumed by reactions with VOCs (68 %) and CO (23 %), while the reactions
363 of OH with NO_2 (7%) and NO (2 %) were negligible. For HO_2 formation, the reaction of
364 RO_2+NO (59%) and the reaction of OH with CO (26%) were the main sources, followed by
365 the reaction of OH with HCHO (9%), HCHO photolysis (5%), and ozonolysis of alkenes (1%)
366 (Figure 5c). Meanwhile, HO_2 was mainly consumed by reacting with NO (74%), followed by
367 the reaction between HO_2 and RO_2 (17%), and the reaction between HO_2 and HO_2 (9%).

368 In comparison, during episodes, the predominant reaction pathways for radical formation and
369 loss were the same as those on non-O_3 episodes, but the radical formation/loss rates for most
370 of the reaction pathways were higher. With the increase of the precursors (*i.e.*, VOC, CO and
371 NO_x; Table 1) and OH radicals (Figure 4) during episodes, the reaction pathways of OH with
372 NO, NO_2, CO and VOC significantly facilitated the OH loss (Figure 5b). The OH loss rates for
373 the pathways of VOC+OH and CO+OH increased ($p<0.05$) by about 1.2 and 2.4 times on
374 episodes, respectively, compared to those on non-O_3 episodes, which promoted the production
375 of peroxy radicals (*i.e.*, RO_2 and HO_2) to accelerate the propagation of the chain reactions.
376 Indeed, in the HO_2 formation pathways, the reaction rate of RO_2+NO doubled during episodes
377 (Figure 5d). Meanwhile, both photolysis of HCHO and reaction of HCHO+OH increased ~66%
378 and ~195% (Figure 5d), respectively, compared to non-O_3 episodes, which also accelerated the

379 HO_2 formation on episode days. Consequently, the reaction rate of HO_2+NO → OH+NO_2 on
380 episodes became 3.6 times that on non-O_3 episodes (shown in both the OH formation pathway
381 in Figure 5b and the HO_2 loss pathway in Figure 5d). As the pathways of both RO_2+NO and
382 HO_2+NO out competed O_3 from the null cycle of NO-NO_2-O_3, it is apparent that O_3 formation
383 was strengthened from non-O_3 episode days to episode days over the SCS.

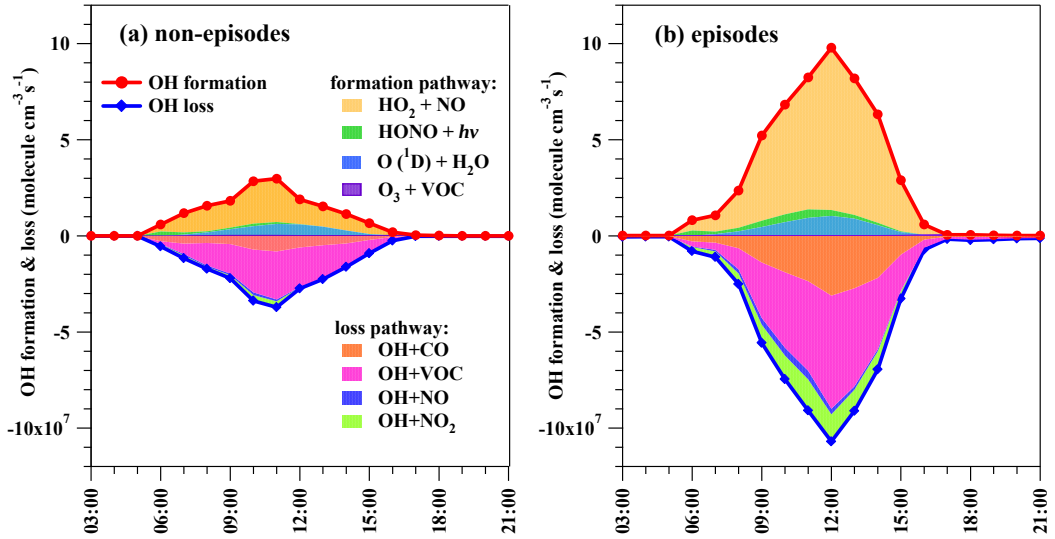

384

385

386 Figure 5. Simulated average formation and loss rates of OH on (a) non-O_3 episodes and (b) O_3
387 episodes, and HO_2 on (c) non-O_3 episodes and (d) O_3 episodes at WSI.

3.4.2 In-situ net O_3 production

Figure 6 depicts the simulated diurnal profiles of O_3 production and destruction rates on episodes and non-O_3 episodes at WSI. Overall, both O_3 production and destruction rates increased on episodes, compared to those on non-O_3 episodes. Further, the O_3 production was significantly greater than the O_3 destruction on both episode and non-O_3 episode days, indicative of net O_3 production over the SCS. In addition, the daytime average net O_3 production rate on episode days (5.7±1.1 ppbv h^{-1}) was much higher than that (1.8±0.4 ppbv h^{-1}) on non-O_3 episode days ($p < 0.05$).

The main pathways of O_3 production and destruction are also displayed in Figure 6. The O_3 production was dominated by the reaction of HO_2 with NO, with an average production rate of 4.7±0.9 ppbv h^{-1} (relative contribution: 63%) and 1.3±0.3 ppbv h^{-1} (53%) on episodes and non-O_3 episodes, respectively, while the NO oxidation by RO_2 accounted for 2.8±0.5 ppbv h^{-1} (37%) and 1.1±0.2 ppbv h^{-1} (47%), respectively. It is noteworthy that RO_2+NO represented more than 1,000 pathways. Hence, the RO_2+NO pathways were further elaborated. Table S2 lists the top 10 pathways of RO_2+NO that contributed to O_3 production on episodes and non-O_3 episodes at WSI. Clearly, CH_3O_2+NO was the main pathway of RO_2+NO, accounting for 31% (production rate: 0.9±0.2 ppbv h^{-1}) on episodes and 46% (0.5±0.1 ppbv h^{-1}) on non-O_3 episodes, respectively. In addition, the reactions of C_2 radicals with NO contributed to 16% (0.4±0.1 ppbv h^{-1}, episodes) and 12% (0.1±0.02 ppbv h^{-1}, non-O_3 episodes), whereas the RO_2 radicals generated from aromatics occupied 10% (0.3±0.1 ppbv h^{-1}, episodes) and 6% (0.07±0.01 ppbv h^{-1}, non-O_3 episodes). In total, the 10 reaction pathways accounted for 57% and 64% of the total pathways of RO_2+NO on episodes and non-O_3 episodes, respectively.

In contrast, the reactions of OH+NO_2 and O_3 photolysis were the major contributors to O_3 destruction on O_3 episode days with an average destruction rate of 0.9±0.2 ppbv h^{-1} (52%) and

412 0.5±0.1 ppbv h^{-1} (29%), respectively, while O_3 photolysis made the highest contribution on
413 non-O_3 episode days (destruction rate: 0.3±0.1 ppbv h^{-1}; relative contribution: 50%), followed
414 by the reactions of OH+NO_2 (0.1±0.1 ppbv h^{-1}; 23%). The different contributors to the O_3
415 destruction were mainly attributed to higher NO_2 level during episodes, which facilitated the
416 production of HNO_3 via the terminal reaction of OH and NO_2. Besides, the reactions of
417 O_3+HO_2, O_3+OH, and the ozonolysis of unsaturated VOCs made minor contributions (17%, 6%
418 and 4% for non-O_3 episodes; 10%, 7% and 2% for episodes, respectively) to the O_3 destruction
419 due to the lower reaction rates of O_3 with radicals and alkenes (< 0.1 ppbv h^{-1} for non-episodes
420 and < 0.2 ppbv h^{-1} for episodes).

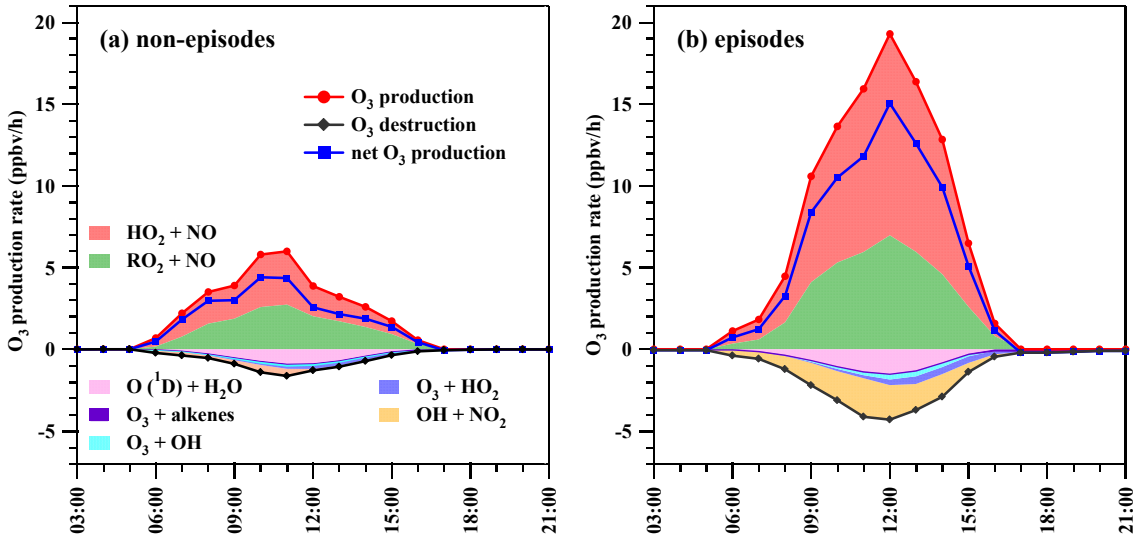

421

422 Figure 6. Breakdown of simulated O_3 production and destruction rates at WSI on (a) non-O_3
423 episodes and (b) episodes. The total production, total destruction and net production rates are
424 red, black and blue lines, respectively.

425 3.4.3 Impact of VOCs on O_3 formation pathways

426 After the most sensitive VOC species to O_3 formation were identified by RIR value, the impact
427 of these selected VOCs on O_3 formation pathways was investigated in detail. As discussed

above, a VOC species can affect the O_3 formation by not only producing RO_2 radicals through reactions with OH, but also generating HO_2 via the cycling processes (SR-10 in Text S1). Thus the pathways of VOCs contributing to O_3 formation can be categorized into two reactions: RO_2+NO and HO_2+NO.

(1). RO_2+NO pathway:

Figure 7 displays simulated contributions of the top 10 VOC species (determined by their RIR values and these 10 VOCs included 9 top AVOC and isoprene) to O_3 formation pathways at WSI during episodes and non-O_3 episodes. The simulated contribution of each VOC was calculated from the difference between two scenarios. One was called "base case", in which all measurement data was input into the PBM-MCM model. The other was "constrained case", which also used all measurement data but excluded the selected one VOC as input. Hence, the contribution of each individual VOC to O_3 formation pathways was obtained from the difference between the output of the "base case" and the related "constrained case" (see Eq. 6 in the footnote of Tables S3 and S4, respectively). In addition, the contributions of the top 10 VOC species to the variations of radicals and NO_x are also specified in Table S3 (for O_3 episodes) and Table S4 (for non-O_3 episodes). During episodes, toluene made the largest contribution to RO_2+NO pathway (9.6%), followed by formaldehyde (9.1%) and acetaldehyde (8.6%) (Figure 7a). In total, the contributions of the 10 major VOCs accounted for 53.6% of the pathway of RO_2+NO. In comparison, during non-O_3 episodes, trimethylbenenze and xylene made the main contributions to RO_2+NO, with a percentage of 4.9% and 4.8%, respectively, followed by toluene (4.2%) and isoprene (3.6%) (Figure 7b). The total contributions of the 10 major VOCs only accounted for 25.4% of the pathway of RO_2+NO. The positive contributions of most VOCs to RO_2+NO pathway can be explained by the variations of radicals and NO. In Tables S3 and S4, it was found that all RO_2 and most HO_2 increased, while all NO and most

OH decreased. Taking toluene as an example (Row 1 in Table S3), toluene consumed OH to produce RO_2 (SR-6 in Text S1), thus OH decreased 2.9% and RO_2 increased 16.7%. Further conversion of RO_2 to HO_2 (SR-10) caused an increase of HO_2 (9.3%). Since both RO_2 and HO_2 consumed NO to produce O_3 (SR-10 and SR-1), NO decreased 3.5%. Thus, the largely increased RO_2 and insignificantly decreased NO resulted in an increasing contribution of toluene to RO_2+NO pathway (9.6%). However, it is worth noting that formaldehyde made a negative contribution to the pathway (-1.5%). According to the reaction SR-12, the reaction of HCHO and OH produced HO_2 and CO directly. HCHO only influences RO_2 indirectly through reactions SR-1 and SR-6. Indeed, with regard to the contribution of HCHO (Row 10 in Table S4), HO_2 increased 12.4% (SR-11 and SR-12) and RO_2 only increased 4.1%, while more NO was consumed (9.6%). The largely decreased NO and insignificantly increased RO_2 led to a decreasing contribution of HCHO to RO_2+NO pathway, presenting a negative contribution.

(2). HO_2+NO pathway:

During episodes, HCHO dominated the contribution to HO_2+NO (18.3%), since HCHO directly produces HO_2 through its photolysis and the reactions with OH (SR-11 and SR-12) (Figure 7a). However, the contributions of other VOCs were less than 5%. The total contributions of the 10 major VOCs accounted for 36.1% of the pathway of HO_2+NO.

In comparison, during non-O_3 episodes, it was found that most VOC species made negative contributions to HO_2+NO pathway (Figure 7b). Acetaldehyde made the most negative contribution (-4.5%), followed by trimethylbenenze (-3.2%), xylene (-1.8%) and toluene (-1.7%). As the conversion of RO_2 to HO_2 was limited by NO during non-O_3 episodes (SR-10), the increase of RO_2 caused little change of HO_2 (See Table S4). Again, using toluene as an example (Row 3 in Table S4), RO_2 increased 7.2% and NO decreased 3.1%, while HO_2 only increased 0.4%. With the little changed HO_2 and a decreased NO, the contributions of most VOCs to the pathway of HO_2+NO decreased, leading to a negative contribution. Nevertheless,

two species had positive contributions to the HO_2+NO pathway. HCHO dominated the contribution of HO_2+NO (5.5%), followed by ethene (1.1%). Since HCHO produced HO_2 directly, it is not surprising to see its contribution to the HO_2+NO pathway. The minor contributions from ethene were due to the chemical characteristics of alkenes. That is, OH radicals are added to its double bond and are not abstracting a hydrogen atom from ethene to produce $HOCH_2CH_2O_2$ radicals (SR-19 in Text S2) (Seinfeld and Pandis, 2006). Furthermore, the $HOCH_2CH_2O$ radicals, products of $HOCH_2CH_2O_2$+NO (SR-20), are easy to decompose (SR-21) and react with O_2 (SR-22, 23) to produce HCHO and HO_2 radicals. The overall reactions (SR-19-23) can be simplified as (Seinfeld and Pandis, 2006):

$$C_2H_4 + OH\cdot + NO \xrightarrow{3O_2} NO_2 + 1.44\ HCHO + 0.28\ HOCH_2CHO + HO_2\cdot \qquad \text{(R-1)}$$

Similarly, propene (the 11th species during episodes, figure not shown) followed the reaction (R-1) with less HCHO produced (the constant was 1.3), resulting in positive but lower contribution to HO_2+NO (0.1%). Overall, although HCHO and ethene made positive contributions to HO_2+NO, the total contribution of the 10 major VOCs was negative, accounting for -7.8% of the pathway of HO_2+NO on non-O_3 episodes.

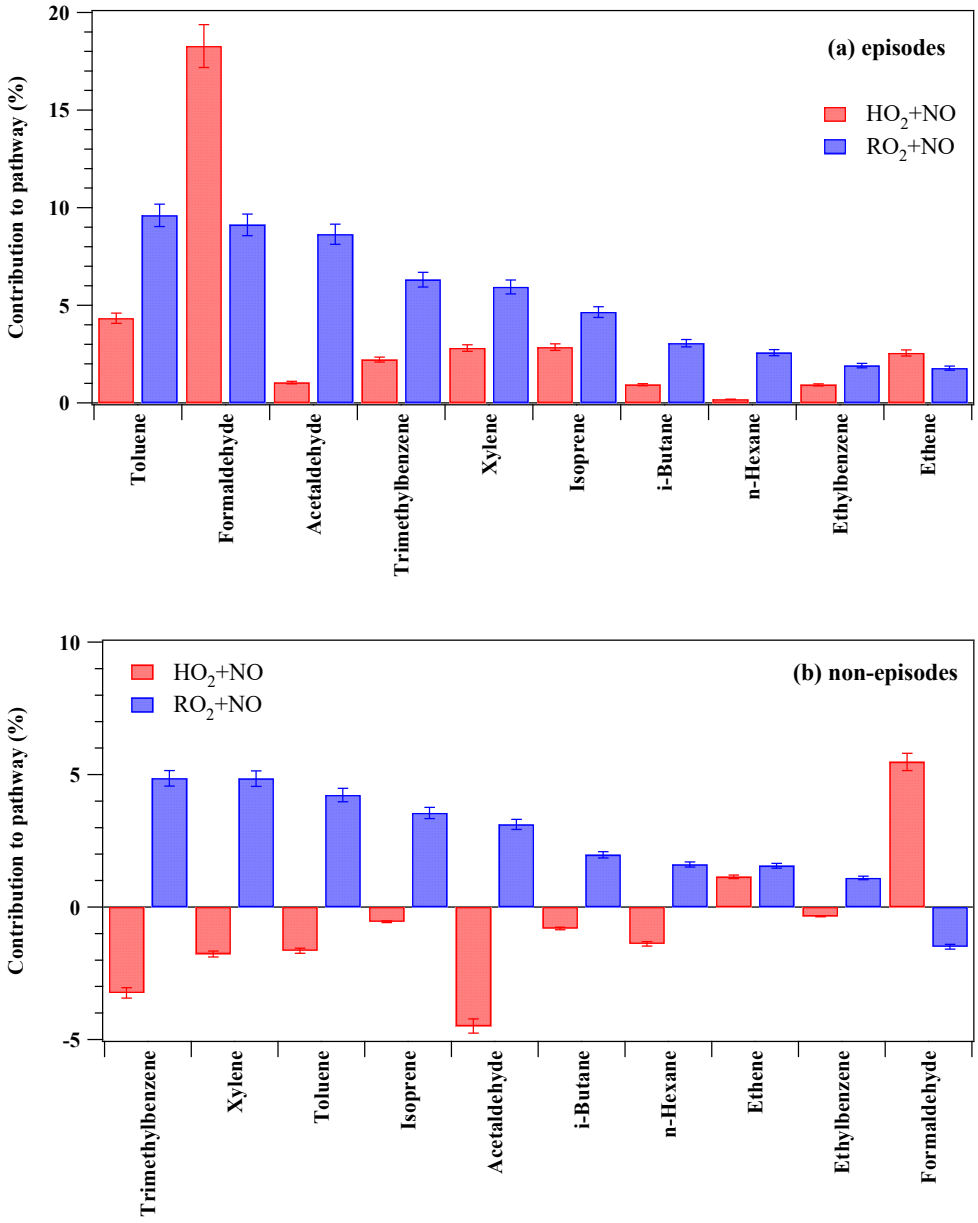

Figure 7. Simulated contributions of top 10 VOC species to O_3 formation pathways at WSI during (a) O_3 episodes and (b) non-O_3 episodes. The top 10 VOC species are determined by their RIR values. Error bars represent 95% confidence interval of the averages.

4 Conclusions

A PBM-MCM model, driven with the observation data obtained in autumn 2013, was used to investigate O_3 photochemistry at WSI over the SCS. Unlike previous studies undertaken in

continental areas of the study region, this study for the first time attempted to understand the O_3 photochemistry over the marine environment under the influence of continental emissions. Compared to non-O_3 episodes, the levels of O_3 and its precursors were significantly higher during episodes. The simulated results revealed that the O_3 formation was VOC-limited on episode days but more sensitive to NO_x during non-O_3 episodes, implying that controlling NO_x emissions during non-episode days was more effective to O_3 reduction, while cutting VOC emissions on episode days mitigated O_3 formation over the SCS. It was found that the summed RIR values of top 10 AVOC species accounted for 77% of the total RIRs, indicating that O_3 formation over the SCS was mainly caused by a few VOC species, especially OVOCs, and the control measures should focus on these species to reduce the O_3 pollution. Analysis of O_3 photochemistry showed that the average OH mixing ratio was $4.2 \pm 1.1 \times 10^6$ molecules cm^{-3} during episodes and $2.5 \pm 0.8 \times 10^6$ molecules cm^{-3} on non-O_3 episode days, reflecting higher photochemical reactivity on episode days. In addition, both the production and loss rates of OH and HO_2 were higher on episodes, suggesting more efficient radical cycling, which led to the O_3 production greater than the O_3 destruction on both episode and non-O_3 episode days, indicative of net O_3 production with a rate of 5.7±1. 1 ppbv h^{-1} on episode days and 1.8±0.4 ppbv h^{-1} on non-O_3 episode days. Moreover, photochemistry of toluene and trimethylbenzene made the highest contribution to the pathway of RO_2+NO during episodes and non-O_3 episodes, respectively, while HCHO chemistry dominated the contribution to HO_2+NO pathway on both episodes and non-O_3 episode days. These findings advanced our knowledge on the O_3 photochemistry over the SCS.

Acknowledgements

This work was funded by the Natural Science Foundation of China (41275122), the Research Grants Council (RGC) of the Hong Kong Government of Special Administrative Region (PolyU5154/13E, PolyU152052/14E, PolyU152052/16E and CRF/C5004-15E), the

Innovation and Technology Commission of the HKSAR to the Hong Kong Branch of National Rail Transit Electrification and Automation Engineering Technology Research Center (1-BBYD), and the Hong Kong Polytechnic University PhD scholarships (project #RTTA). This study is supported in part by the Hong Kong PolyU internal grant (1-BBW4 and 4-ZZFW).

Refernces

Cardelino, C.A., Chameides, W.L., 1995. An observation-based model for analyzing ozone precursor relationships in the urban atmosphere. Journal of the Air and Waste Management 45, 161-180.

Chan, L.Y., Chan, C.Y., Qin, Y., 1998a. Surface ozone pattern in Hong Kong. Journal of Applied Microbiology 37, 1153-1165.

Chan, L.Y., Liu, H.Y., Lam, K.S., Wang, T., Oltmans, S.J., Harris, J.M., 1998b. Analysis of the seasonal behavior of tropospheric ozone at Hong Kong. Atmospheric Environment 32, 159-168.

Cheng, H.R., Guo, H., Saunders, S.M., Lam, S.H.M., Jiang, F., Wang, X.M., Simpson, I.J., Blake, D.R., Louie, P.K.K., Wang, T.J., 2010a. Assessing photochemical ozone formation in the Pearl River Delta with a photochemical trajectory model. Atmospheric Environment 44, 4199-4208.

Cheng, H.R., Guo, H., Wang, X.M., Saunders, S.M., Lam, S.H., Jiang, F., Wang, T.J., Ding, A.J., Lee, S.C., Ho, K.F., 2010b. On the relationship between ozone and its precursors in the Pearl River Delta: application of an observation-based model (OBM). Environmental Science and Pollution Research International 17, 547-560.

Curtis, A.R., Sweetenham, W.P., 1987. FACSIMILE release H user's manual. AERE Report R11771 (HMSO), London.

Derwent, R., 2017. Intercomparison of chemical mechanisms for air quality policy formulation and assessment under North American conditions. Journal of the Air and Waste Management Association 67, 789-796.

Ding, A.J., Wang, T., Zhao, M., Wang, T.J., Li, Z.K., 2004. Simulation of sea-land breezes and a discussion of their implications on the transport of air pollution during a multi-day ozone episode in the Pearl River Delta of China. Atmospheric Environment 38, 6737-6750.

Finlayson-Pitts, B.J., Pitts, J.N., 1993. Atmospheric Chemistry of Tropospheric Ozone Formation: Scientific and Regulatory Implications. Air and Waste 43, 1091-1100.

Guo, H., Ling, Z.H., Cheng, H.R., Simpson, I.J., Lyu, X.P., Wang, X.M., Shao, M., Lu, H.X., Ayoko, G., Zhang, Y.L., Saunders, S.M., Lam, S.H.M., Wang, J.L., Blake, D.R., 2017. Tropospheric volatile organic compounds in China. Science of the Total Environment 574, 1021-1043.

Guo, H., Jiang, F., Cheng, H.R., Simpson, I.J., Wang, X.M., Ding, A.J., Wang, T.J., Saunders, S.M., Wang, T., Lam, S.H.M., Blake, D.R., Zhang, Y.L., Xie, M., 2009. Concurrent observations of air pollutants at two sites in the Pearl River Delta and the implication of regional transport. Atmospheric Chemistry and Physics 9, 7343-7360.

Guo, H., Ling, Z.H., Cheung, K., Jiang, F., Wang, D.W., Simpson, I.J., Barletta, B., Meinardi, S., Wang, T.J., Wang, X.M., Saunders, S.M., Blake, D.R., 2013. Characterization of photochemical pollution at different elevations in mountainous areas in Hong Kong. Atmospheric Chemistry and Physics 13, 3881-3898.

Guo, H., Wang, T., Blake, D.R., Simpson, I.J., Kwok, Y.H., Li, Y.S., 2006. Regional and local contributions to ambient non-methane volatile organic compounds at a polluted rural/coastal site in Pearl River Delta, China. Atmospheric Environment 40, 2345-2359.

Guo, H., So, K.L., Simpson, I.J., Barletta, B., Meinardi, S., Blake, D.R., 2007. C_1–C_8 volatile organic compounds in the atmosphere of Hong Kong: Overview of atmospheric processing and source apportionment. Atmospheric Environment 41, 1456-1472.

Guo, H., Cheng, H.R., Ling, Z.H., Louie, P.K., Ayoko, G.A., 2011. Which emission sources are responsible for the volatile organic compounds in the atmosphere of Pearl River Delta? Journal of Hazardous Materials 188, 116-124.

Han, J., Shin, B., Lee, M., Hwang, G., Kim, J., Shim, J., Lee, G., Shim, C., 2015. Variations of surface ozone at Ieodo Ocean Research Station in the East China Sea and the influence of Asian outflows. Atmospheric Chemistry and Physics 15, 12611-12621.

Huang, J.P., Fung, J.C.H., Lau, A.K.H., Qin, Y., 2005. Numerical simulation and process analysis of typhoon-related ozone episodes in Hong Kong. Journal of Geophysical Research 110, D05301.

Jiang, F., Guo, H., Wang, T.J., Cheng, H.R., Wang, X.M., Simpson, I.J., Ding, A.J., Saunders, S.M., Lam, S.H.M., Blake, D.R., 2010. An ozone episode in the Pearl River Delta: Field observation and model simulation. Journal of Geophysical Research 115, D22305.

Jacob, D. J., 1999, Introduction to Atmospheric Chemistry, Princeton University Press, Princeton, New Jersey.

Jenkin, M.E., Saunders, S.M., Pilling, M.J., 1997. The tropospheric degradation of volatile organic compounds: a protocol for mechanism development. Atmospheric Environment 31, 81-104.

Jenkin, M.E., Saunders, S.M., Wagner, V., Pilling, M.J., 2003. Protocol for the development of the Master Chemical Mechanism, MCM v3 (Part B): tropospheric degradation of aromatic volatile organic compounds. Atmospheric Chemistry and Physics 3, 181-193.

Lam, S.H.M., Saunders, S.M., Guo, H., Ling, Z.H., Jiang, F., Wang, X.M., Wang, T.J., 2013. Modelling VOC source impacts on high ozone episode days observed at a mountain summit in Hong Kong under the influence of mountain-valley breezes. Atmospheric Environment 81, 166-176.

Lee, Y.C., Calori, G., Hills, P., Carmichael, G.R., 2002. Ozone episodes in urban Hong Kong 1994–1999. Atmospheric Environment 36, 1957-1968.

Ling, Z.H., Guo, H., Lam, S.H.M., Saunders, S.M., Wang, T., 2014. Atmospheric photochemical reactivity and ozone production at two sites in Hong Kong: Application of a Master Chemical Mechanism-photochemical box model. Journal of Geophysical Research 119, 10567–10582.

Ling, Z.H., Guo, H., Zheng, J.Y., Louie, P.K.K., Cheng, H.R., Jiang, F., Cheung, K., Wong, L.C., Feng, X.Q., 2013. Establishing a conceptual model for photochemical ozone pollution in subtropical Hong Kong. Atmospheric Environment 76, 208-220.

Liu, Y., Shao, M., Lu, S.H., Liao, C.C., Wang, J.L., Chen, G., 2008. Volatile organic compound (VOC) measurements in the pearl river delta (PRD) region, China. Atmospheric Chemistry and Physics 8, 1531-1545.

Long, B., Bao, J.L., Truhlar, D.G., 2017. Reaction of SO_2 with OH in the atmosphere. Physical Chemistry Chemical Physics 19, 8091-8100.

Lou, S., Holland, F., Rohrer, F., Lu, K., Bohn, B., Brauers, T., Chang, C.C., Fuchs, H., Häseler, R., Kita, K., Kondo, Y., Li, X., Shao, M., Zeng, L., Wahner, A., Zhang, Y., Wang, W., Hofzumahaus, A., 2010. Atmospheric OH reactivities in the Pearl River Delta – China in summer 2006: measurement and model results. Atmospheric Chemistry and Physics 10, 11243-11260.

Lu, K.D., Rohrer, F., Holland, F., Fuchs, H., Bohn, B., Brauers, T., Chang, C.C., Häseler, R., Hu, M., Kita, K., Kondo, Y., Li, X., Lou, S.R., Nehr, S., Shao, M., Zeng, L.M., Wahner, A., Zhang, Y.H., Hofzumahaus, A., 2012. Observation and modelling of OH and HO_2 concentrations in the Pearl River Delta 2006: a missing OH source in a VOC rich atmosphere. Atmospheric Chemistry and Physics 12, 1541-1569.

Lu, K.D., Rohrer, F., Holland, F., Fuchs, H., Brauers, T., Oebel, A., Dlugi, R., Hu, M., Li, X., Lou, S.R., Shao, M., Zhu, T., Wahner, A., Zhang, Y.H., Hofzumahaus, A., 2014. Nighttime observation and chemistry of HO_x in the Pearl River Delta and Beijing in summer 2006. Atmospheric Chemistry and Physics 14, 4979-4999.

Lu, K. D., Zhang, Y. H., Su, H., Shao, M., Zeng, L. M., Zhong, L. J., Xiang, Y. R., Chang, C. C., Chou, C.K.C., Wahner, A., 2010. Regional ozone pollution and key controlling factors of photochemical ozone production in Pearl River Delta during summer time. Science China Chemistry 53, 651-663.

Lyu, X.P., Liu, M., Guo, H., Ling, Z.H., Wang, Y., Louie, P.K.K., Luk, C.W.Y., 2016a. Spatiotemporal variation of ozone precursors and ozone formation in Hong Kong: Grid field measurement and modelling study. Science of the Total Environment 569, 1341-1349.

Lyu, X.P., Guo, H., Simpson, I.J., Meinardi, S., Louie, P.K.K., Ling, Z.H., Wang, Y., Liu, M., Luk, C.W.Y., Wang, N., Blake, D.R., 2016b. Effectiveness of replacing catalytic converters in LPG-fueled vehicles in Hong Kong. Atmospheric Chemistry and Physics 16, 6609-6626.

Lyu, X.P., Chen, N., Guo, H., Zhang, W.H., Wang, N., Wang, Y., Liu, M., 2015a. Ambient volatile organic compounds and their effect on ozone production in Wuhan, central China. Science of the Total Environment 541, 200-209.

Lyu, X.P., Ling, Z.H., Guo, H., Saunders, S.M., Lam, S.H.M., Wang, N., Wang, Y., Liu, M., Wang, T., 2015b. Re-examination of C_1–C_5 alkyl nitrates in Hong Kong using an observation-based model. Atmospheric Environment 120, 28-37.

NARSTO, 2000. An Assessment of Tropospheric Ozone Pollution —A North American Perspective. NARSTO Management Office (Envair), Pasco, Washington.

NRC, 1991. Rethinking the Ozone Problem in Urban and Regional Air Pollution. The National Academies Press, Washington, DC.

Ou, J.M., Guo, H., Zheng, J.Y., Cheung, K., Louie, P.K.K., Ling, Z.H., Wang, D.W., 2015. Concentrations and sources of non-methane hydrocarbons (NMHCs) from 2005 to 2013 in Hong Kong: A multi-year real-time data analysis. Atmospheric Environment 103, 196-206.

Ou Yang, C. F., Hsieh, H. C., Wang, S. H., Lin, N. H., Lee, C. T., Sheu, G. R., Wang, J. L., 2013. Influence of Asian continental outflow on the regional background ozone level in northern South China Sea. Atmospheric Environment 78, 144-153.

Saunders, S.M., Jenkin, M.E., Derwent, R.G., Pilling, M.J., 2003. Protocol for the development of the Master Chemical Mechanism, MCM v3 (Part A): tropospheric degradation of non-aromatic volatile organic compounds. Atmospheric Chemistry and Physics 3, 161-180.

Seinfeld, J. H., and S. N. Pandis, 2006. Atmospheric Chemistry and Physics: From Air Pollution to Climate Change, 2nd Edn., 1232 pp.,Wiley, N. J.

Simpson, I.J., Blake, N.J., Barletta, B., Diskin, G.S., Fuelberg, H.E., Gorham, K., Huey, L.G., Meinardi, S., Rowland, F.S., Vay, S.A., Weinheimer, A.J., Yang, M., Blake, D.R., 2010. Characterization of trace gases measured over Alberta oil sands mining operations: 76 speciated C_2-C_{10} volatile organic compounds (VOCs), CO_2, CH_4, CO, NO, NO_2, NO_y, O_3 and SO_2. Atmospheric Chemistry and Physics 10, 11931-11954.

Solberg, S., Simpson, D., Jonson, J. E., Hjellbrekke, A. G., Derwent, R., 2004. EMEP Assessment, Part 1, European Perspective, 6.1 The oxidant formation process and its long range transport, Berlin, October 2004. http://www.bioone.org/doi/abs/10.1579/0044-7447-34.1.2.

Wang, T., Poon, C.N., Kwok, Y.H., Li, Y.S., 2003. Characterizing the temporal variability and emission patterns of pollution plumes in the Pearl River Delta of China. Atmospheric Environment 37, 3539-3550.

Wang, Y., Wang, H., Guo, H., Lyu, X., Cheng, H., Ling, Z., Louie, P.K.K., Simpson, I.J., Meinardi, S., Blake, D.R., 2017a. Long-term O_3–precursor relationships in Hong Kong: field observation and model simulation. Atmospheric Chemistry and Physics 17, 10919-10935.

Wang, X., Zhang, Y., Hu, Y., Zhou, W., Lu, K., Zhong, L., Zeng, L., Shao, M., Hu, M., Russell, A.G., 2010. Process analysis and sensitivity study of regional ozone formation over the Pearl River Delta, China, during the PRIDE-PRD2004 campaign using the Community Multiscale Air Quality modeling system. Atmospheric Chemistry and Physics 10, 4423-4437.

Wang, H., Lyu, X. P., Guo, H., Wang, Y., Zou, S. C., Ling, Z. H., Jiang, F., Wang, X. M., Zeren, Y. Z., Pan, W. Z., 2017b. Ozone pollution around a coastal region of South China Sea: Interaction between marine and continental air masses. Submitted to Atmospheric Chemistry and Physics (In review)

679 Wang, T., Guo, H., Blake, D.R., Kwok, Y.H., Simpson, I.J., Li, Y.S., 2005. Measurements of
680 Trace Gases in the Inflow of South China Sea Background Air and Outflow of Regional
681 Pollution at Tai O, Southern China. Journal of Atmospheric Chemistry 52, 295-317.

682 Wang, N., Guo, H., Jiang, F., Ling, Z.H., Wang, T., 2015. Simulation of ozone formation at
683 different elevations in mountainous area of Hong Kong using WRF-CMAQ model. Science of
684 the Total Environment 505, 939-951.

685 Xue, L.K., Gu, R.R., Wang, T., Wang, X.F., Saunders, S., Blake, D., Louie, P.K.K., Luk,
686 C.W.Y., Simpson, I., Xu, Z., Wang, Z., Gao, Y., Lee, S.C., Mellouki, A., Wang, W.X., 2016.
687 Oxidative capacity and radical chemistry in the polluted atmosphere of Hong Kong and Pearl
688 River Delta region: analysis of a severe photochemical smog episode. Atmospheric Chemistry
689 and Physics 16, 9891-9903.

690 Zhang, J., Wang, T., Chameides, W.L., Cardelino, C., Kwok, J., Blake, D.R., Ding, A., So,
691 K.L., 2007. Ozone production and hydrocarbon reactivity in Hong Kong, Southern China.
692 Atmospheric Chemistry and Physics 7, 557-573.

693 Zhang, Y.H., Hu, M., Zhong, L.J., Wiedensohler, A., Liu, S.C., Andreae, M.O., Wang, W.,
694 Fan, S.J., 2008. Regional Integrated Experiments on Air Quality over Pearl River Delta 2004
695 (PRIDE-PRD2004): Overview. Atmospheric Environment 42, 6157-6173.

696 Zhang, Y., Wang, X., Blake, D.R., Li, L., Zhang, Z., Wang, S., Guo, H., Lee, F.S.C., Gao, B.,
697 Chan, L., Wu, D., Rowland, F.S., 2012. Aromatic hydrocarbons as ozone precursors before
698 and after outbreak of the 2008 financial crisis in the Pearl River Delta region, south China.
699 Journal of Geophysical Research: Atmospheres 117, D15306.